



**MOHAMED  
HADDADI**

**Structured light generation using spatial light  
modulators**





**MOHAMED  
HADDADI**

**Geração de luz estruturada com uso de moduladores  
espaciais de luz**

Projeto final apresentado à Universidade de Aveiro para cumprimento dos requisitos necessários à obtenção do grau de Licenciatura em Física, realizado sob a orientação científica do Doutor Gil Fernandes, Investigador no Instituto de Telecomunicações.



## **o júri**

Presidente

**Prof. Doutor Manuel Barroso**

Professor associado da Universidade de Aveiro

Arguente

**Prof. Doutora Ana Maria Rocha**

Investigadora no Instituto de Nanoestruturas, Nanomodelação e Nanofabricação da Universidade de Aveiro

Orientador

**Doutor Gil Gonçalo Martins Fernandes**

Investigador no Instituto de Telecomunicações da Universidade de Aveiro



## **agradecimentos**

Primeiramente gostaria de agradecer ao meu orientador Dr. Gil Fernandes por todo o apoio oferecido ao longo do desenvolvimento deste trabalho, este projeto não seria possível sem a sua partilha de conhecimento e disponibilidade para ajudar na solução dos problemas que surgiram. Agradeço ao Instituto de Telecomunicações e à Universidade de Aveiro por terem facilitado todas as condições necessárias para a realização deste trabalho experimental. Por fim quero agradecer à minha família, em especial minha mãe, por todo o apoio e ajuda dados durante esta etapa.





## **palavras-chave**

Luz Estruturada, feixes Hermite-Gaussianos, feixes Laguerre-Gaussianos, feixes de Bessel-Gaussianos, momento angular orbital (OAM), Moduladores Espaciais de Luz (SLMs).

## **Resumo**

Este estudo explora a geração e análise de feixes de luz estruturada, com foco específico nos feixes Hermite-Gaussianos, Laguerre-Gaussianos e de Bessel-Gauss, bem como nas suas soluções que transportam Momento Angular Orbital (OAM). Utilizando Moduladores Espaciais de Luz (SLMs), esses feixes são produzidos experimentalmente, e a sua intensidade espacial é capturada por um perfilador de feixe de laser (LBP). Os resultados experimentais são então comparados com seus equivalentes teóricos. O principal objetivo deste projeto inclui melhorar a pureza dos feixes gerados para aumentar sua aplicabilidade em sistemas de comunicação ótica. Finalmente, uma interface gráfica de usuário foi desenvolvida, permitindo a criação dos feixes referidos assim como a sua caracterização em tempo real e comparação com o perfil de intensidades teórico.



**keywords**

Structured Light, Hermite-Gaussian beams, Laguerre-Gaussian beams, Bessel-Gaussian beams, orbital angular momentum (OAM), Spatial Light Modulators (SLMs).

**Abstract**

This study explores the generation and analysis of structured light beams, specifically focusing on Hermite-Gaussian, Laguerre-Gaussian, and Bessel-Gaussian beams, as well as their solutions that carry Orbital Angular Momentum (OAM). Utilizing Spatial Light Modulators (SLMs), these beams are experimentally produced, and their spatial intensity is captured by a laser beam profiler (LBP). The experimental results are then compared to their theoretical counterparts. The main objective of this project includes improving the purity of generated beams to enhance their applicability in optical communication systems. Finally, a graphical user interface was developed, enabling the creation of any of these aforementioned optical beams using an SLM and providing real-time visualization of the generated beam and the theoretical intensity profile.



# Index

TABLE OF FIGURES .....	III
ACRONYM LIST .....	V
<b>1. INTRODUCTION .....</b>	<b>1</b>
1.1 STRUCTURED LIGHT .....	1
1.2 ORBITAL ANGULAR MOMENTUM.....	2
1.3 OBJECTIVES.....	3
1.4 DOCUMENT’S STRUCTURE.....	3
<b>2. THEORETICAL BACKGROUND .....</b>	<b>4</b>
2.1 PARAXIAL HELMHOLTZ EQUATION: .....	4
2.2 STRUCTURED LIGHT BEAMS .....	6
2.2.1 Gaussian beams.....	6
2.2.2 Laguerre-Gaussian beams: .....	8
2.2.3 Hermite-Gaussian beams: .....	8
2.2.4 Bessel-Gaussian beams: .....	9
2.3 ORBITAL ANGULAR MOMENTUM.....	10
2.4 BEAM PROPAGATION .....	11
2.4.1 Fresnel diffraction integral .....	11
2.4.2 Fraunhofer Diffraction.....	12
<b>3. STRUCTURED LIGHT MANIPULATION: AN OVERVIEW .....</b>	<b>13</b>
3.1 IN FIBERS .....	13
3.1.1 Long-Period Fiber Grating.....	13
3.1.2 Chiral-Long-Period Fiber Grating .....	14
3.2 IN FREE SPACE.....	14
3.2.1 Optical elements .....	14
3.2.1.1 Axicons .....	15
3.2.1.2 Cylindrical lenses.....	15
3.2.1.3 Spiral phase Plates.....	16
3.2.2 Q-Plates.....	16
3.3 SPATIAL LIGHT MODULATORS.....	17
3.3.1 Structure and Operation Principles .....	17
3.3.2 Advantages and Disadvantages .....	19
<b>4. EXPERIMENTAL GENERATION OF STRUCTURED LIGHT.....</b>	<b>20</b>
4.1 EXPERIMENTAL SETUP .....	20
4.1.1 Phase masks .....	21
4.2 GRAPHICAL USER INTERFACE.....	22
4.2.1 Alignment and light modulation .....	22
4.3 EXPERIMENTAL RESULTS .....	24
4.4 ENHANCING OAM GENERATION .....	26
<b>5. CONCLUSIONS .....</b>	<b>28</b>
5.1 FUTURE WORK.....	28
<b>REFERENCES .....</b>	<b>29</b>



# Table of Figures

Figure 1-1 Representation of Spin and orbital angular momentum interaction with matter [8].	2
Figure 2-1 Schematic diagram of Gaussian beam propagation [13].	7
Figure 2-2 Transverse intensity distributions of typical structured light beams beyond the paraxial approximation. Shown from left to right are the cases of the fundamental Gaussian beam, the $H - G_{11}$ , $L - G_{11}$ and $B - G_1$ beams, respectively [14].	9
Figure 3-1 Principle of the controllable all-fiber OAM beam converter [19].	14
Figure 3-2- Schematic diagram for zero-order Bessel generation by Axicon, where $\gamma$ is the base angle of the axicon [22].	15
Figure 3-3 – The cylindrical lens mode converter for the conversion of a $H-G$ $x = 1, y = 0$ mode into the corresponding $L-G$ mode with $l = 1$ and $p = 0$ . The lenses of focal length $f$ are separated by $f/2$ [24].	15
Figure 3-4 Sketch of the spiral phase plate. The top surface spirals upward from height $h_0$ to $h_0 + h_s$ [25].	16
Figure 3-5 - Q-plate working principle: a pictorial representation of equation (3.6) in the optimal case $\Delta = \pi$ [26].	17
Figure 3-6 Typical structure of a reflective LC-SLM [30].	18
Figure 3-7 The structure of a single cell is shown at an expanded scale [31].	18
Figure 4-1 (a) Experimental set up used for manipulating light (b) Schema of the experimental set up. 1 - SLM, 2 - Collimator, 3- DFB, 4 - LBP, 5- Breadboard, 6- Beam splitter, 7- Polarization controller	20
Figure 4-2 (a) - A combination of the phase distribution of the desired optical component (left) plus a linear phase ramp (middle) creates a forked diffraction grating (right), which can produce a helically phased beam. In this case $l = 3$ [32]. (b) - When a standard laser beam illuminates a forked diffraction grating, the first-order diffracted beam has helical phase fronts [33].	22
Figure 4-3 On the left, the functional flow diagram illustrates the alignment operation, detailing the sequential steps involved. On the right, a GUI screenshot highlights the alignment processes, providing a visual representation of the procedural steps	23
Figure 4-4 Progress of wavefront modulation with polarization variation for Horizontal (H) and Vertical (V) beam modulation.	23
Figure 4-5 On the left, the functional flow diagram illustrates the main operations, detailing the sequential steps involved. On the right, a GUI screenshot highlights the important processes, providing a visual representation of the procedural steps.	24
Figure 4-6 H-G beams results – First row shows the phase mask used, blue-0 and red- $2\pi$ , second row shows the results, and the third one gives the experimental results. H-G orders: (2,0), (1,1), (2,1), (3,3) from the left to the right.	24
Figure 4-7 L-G beams results – First row shows the phase mask used, blue-0 and red- $2\pi$ , second row shows the results, and the third one gives the experimental results. L-G orders: (0,1), (1,1), (2,1), (2,2) from the left to the right.	25
Figure 4-8 B-G beams results – First row shows the phase mask used, blue-0 and red- $2\pi$ , second row shows the results, and the third one gives the experimental results. B-G orders: 0, 1, 2, 3 from the left to the right.	26
Figure 4-9 Improved L-G beams results – First row shows the phase mask used, blue-0 and red- $2\pi$ , second row shows the results, and the third one gives the experimental results. L-G orders: (0,1), (1,1), (2,1), (2,2) and scale parameters 100, 80, 85, 110 from the left to the right.	26
Figure 4-10 The progress of OAM-carrying beam with the increase of grating division in the forked phase mask, $l=1$ .	27
Figure 4-11 Beams carrying OAM, topological charges from 1 to 5.	27





# Acronym List

<b>B-G</b>	Bessel Gaussian
<b>CLPFG</b>	chiral-long-period-fiber-grating
<b>DES</b>	Data-Encoding System
<b>GUI</b>	Graphical User Interface
<b>H-G</b>	Hermite Gaussian
<b>LCoS</b>	Liquid Crystal on Silicon
<b>LPFG</b>	Long-period-fiber-grating
<b>L-G</b>	Laguerre Gaussian
<b>MDM</b>	Mode-Division Multiplexing
<b>OAM</b>	Orbital Angular Momentum
<b>SAM</b>	Spin Angular Momentum
<b>SLM</b>	Spatial Light Modulators



# CHAPTER 1

## Introduction

Human vision is limited to perceiving light intensity, leaving the phase of light invisible to our eyes. As a result, traditional image projection systems have focused solely on modulating light intensity. However, the forefront of light shaping research has shifted towards scenarios and applications in which the phase structuring of the light beam is crucial [1].

Holography exemplifies the importance of spatial phase structure. In holography, light scattered from an object interferes with a spatially coherent plane-wave reference beam, capturing both intensity and phase information. This interference pattern is typically recorded on high-resolution photographic film, which, when illuminated by the same reference light, recreates a visual replica of the object. The development of digital holography, utilizing diffractive optical elements, has expanded its applications, underscoring the ongoing significance of phase structuring in advancing light-based technologies. The contemporary interest in phase structuring can be traced back to 1992, following a seminal paper by Allen and colleagues [2]. They proposed that light beams with a helical phase structure, such as Laguerre-Gaussian laser modes, possess "orbital angular momentum" (OAM), which is distinct from the spin angular momentum of light. This hypothesis was swiftly validated by Rubinsztein-Dunlop and other researchers [3], who demonstrated the transfer of this angular momentum to microscopic particles in optical tweezers, causing them to rotate.

Early experiments utilized photographic film holograms to generate helically phased beams when illuminated with a Gaussian reference beam [4]. Innovatively, Grier and colleagues later replaced the film with a pixelated liquid-crystal phase modulator, allowing dynamic creation of helically phased and other complex beam structures [5]. This advancement in spatial light modulators (SLMs) revolutionized the generation of such beams, extending their applications far beyond optical tweezers. Over the past two decades, the adoption of SLMs has significantly expanded the study and application of non-Gaussian laser beams. These advancements have influenced a wide range of fields, including optical phenomena research, imaging techniques, optical communications, sensing technologies, and quantum science. The versatility and ease of generating complex light beams with SLMs have solidified their role as a cornerstone in exploring and utilizing light's phase properties.

### 1.1 Structured light

Structured light involves the deliberate manipulation of light across its various properties. This manipulation can include shaping light in terms of its timing and frequency to generate precise pulses, or more commonly, controlling its characteristics such as the spatial intensity profile, polarization, and phase. Enabling advancements in fields such as optical communication, microscopy, quantum information, and laser machining. Several types of structured light beams have been experimentally investigated due to their unique properties, particularly in the field of optical communications, including:

- Bessel-Gaussian (B-G) beams possess the remarkable capability to maintain their shape during propagation, thereby minimizing dispersion and preserving signal integrity. This attribute is a very interesting solution for free space optical communications over long distances, particularly under challenging weather conditions. Their distinctive "self-healing" property enables them to recover from disruptions. When B-G beams encounter obstacles or turbulence along their trajectory, they could diffract around these disturbances and subsequently restore their original shape and intensity profile. This ensures continuous and reliable signal transmission despite the presence of such disruptions [6].
- Laguerre-Gaussian (L-G) and Hermite-Gaussian (H-G) beams play pivotal roles in the exploration of OAM in optics. L-G beams, characterized by their distinctive helical phase structure, impart discrete OAM, a property crucial for advancing optical communication and quantum information technologies. While HG beams do not inherently carry OAM, they can be transformed into LG modes, thereby facilitating OAM studies. These complementary beam types offer versatile frameworks, propelling our understanding and practical application of OAM across diverse technological domains [7].

## 1.2 Orbital Angular Momentum

An electromagnetic wave can carry both energy and momentum, comprising linear momentum ( $P$ ) and angular momentum ( $L$ ) that describes the rotational motion and can be conceptualized as the amount of rotation a particle or wave carries.  $L$  can be further divided into two components: polarization spin angular momentum (SAM) and orbital angular momentum (OAM), associated with the spatial distribution of the light field. SAM arises from the polarization of the electromagnetic wave, describing the intrinsic angular momentum per photon associated with its circular polarization states, in contrast to linear momentum, which relates to the directional motion of the wave, SAM is tied to the internal property of the wave, specifically its polarization. OAM, on the other hand, refers to a property of light beams where the photons possess a helical phase front, causing the light to twist around its axis of propagation. This helical structure imparts an angular momentum to the photons, distinct from the SAM associated with polarization, see Figure 1-1. The helical phase front of OAM beams results in a phase singularity along the axis of propagation, leading to a characteristic doughnut-shaped intensity profile.

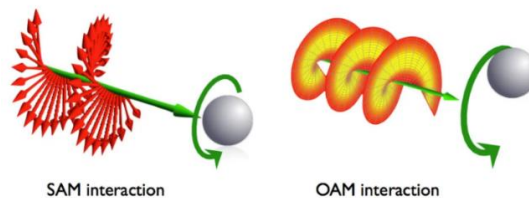


*Figure 1-1 Representation of Spin and orbital angular momentum interaction with matter [8].*

OAM can be quantified on multiple discrete values of  $l$ , or modes, which theoretically allows for a multitude of states. This capability is valuable in various critical applications, especially in

optical communications. In optical communications, OAM can be exploited in two main ways, both in free space and in optical fibers:

- OAM Multiplexing - OAM allows multiple spatial orthogonal channels of information to be transmitted, significantly increasing data transmission capacity. Light is encoded with different values of OAM, which can take an infinite number of values. Each OAM beam can carry information, thus allowing the simultaneous transmission of multiple channels on the same waveguide or free-space channel[9]. However, OAM multiplexing technology still faces several technical challenges, such as the complexity of generating and detecting light beams with OAM and the impact of atmospheric turbulence on transmission quality.
- OAM encoding - This system employs  $N$  distinct OAM states to encode  $N$  symbols, denoted as "0," "1," ..., " $N-1$ ". A sequence of OAM states is generated, with each state transmitted at a different time interval. Upon reaching the receiver, the information can be readily decoded by identifying the received OAM state at each time point.

## 1.3 Objectives

The main objectives of this work are to develop an experimental setup capable of manipulating light to produce different types of beams, including L-G, H-G, and B-G beams, and to integrate it with an intuitive graphical interface. To achieve this, we will use a SLM, which can modulate the phase of the wave, to shape the wavefront using phase masks that will transform an incident Gaussian beam into one of the aforementioned beam types. To verify the results, the experimental outcomes are compared with the theoretical predictions by simulating the beam propagation in free space. Finally, we aim to improve the purity of the OAM beams by exploring the first order diffraction of forked masks.

## 1.4 Document's Structure

This document is structured into five chapters. Chapter 2 delves into the theoretical foundations of structured light, exploring concepts such as L-G, H-G, and B-G beams, along with the principles of OAM. Chapter 3 provides an in-depth examination of various techniques used to generate structured light, including the generation of L-G, H-G, and B-G beams and beams carrying OAM, discussing the principles behind each method. Chapter 4 describes the experimental setup developed for this study, including the optical components and software used for generating and analyzing structured light, including the graphical user interface (GUI) developed for controlling the experimental setup and collecting data. It also presents the results of the beam generation experiments, analyzing the purity of the generated beams and comparing them with theoretical predictions. Finally, Chapter 5 summarizes the study's findings and discusses their implications for communication technologies, offering a detailed discussion of the experimental results and highlighting areas for future research and development in structured light generation and its applications in communication systems.

## CHAPTER 2

# Theoretical Background

This chapter establishes the theoretical underpinnings essential for understanding optical beam propagation, crucial in the field of optics. Starting from Maxwell's equations, which form the foundation for describing the behavior of electromagnetic waves in vacuum, we derive the Helmholtz equation. This equation governs the propagation of electromagnetic waves in media devoid of sources or losses, setting the stage for exploring various beam solutions. We delve into specific solutions such as Gaussian beams, HG, LG, and B-G beams. Each of these solutions offers unique intensity distributions and spatial structures, defining the characteristics of light waves in different scenarios. The introduction of OAM in light beams highlights how phase distributions contribute to the distinct properties observed in these beams. Lastly, mathematical tools such as Fresnel and Fraunhofer diffraction integrals, alongside convolution techniques, are discussed for their pivotal role in modeling and simulating optical beam propagation across diverse scenarios.

In summary, this chapter provides a structured overview of the fundamental principles and practical implications of optical beam propagation. It emphasizes the theoretical groundwork necessary to better understand the field of structured light.

## 2.1 Paraxial Helmholtz equation:

Maxwell's equations are fundamental equations in classical electromagnetism. They describe how electric and magnetic fields interact and propagate in space, and they can be written as,

$$\nabla \cdot \mathbf{E} = 0, \quad (2.1)$$

$$\nabla \cdot \mathbf{B} = 0, \quad (2.2)$$

$$\nabla \times \mathbf{E} = -\frac{\partial \mathbf{B}}{\partial t}, \quad (2.3)$$

$$\nabla \times \mathbf{B} = \mu_0 \epsilon_0 \frac{\partial \mathbf{E}}{\partial t}, \quad (2.4)$$

where  $\mathbf{E}$  and  $\mathbf{B}$  denoting the electric field and magnetic field, respectively, for simplicity of notation, dependence of the fields on position  $\mathbf{r} = x\hat{i} + y\hat{j} + z\hat{k}$ , and time  $t$  is omitted.  $\epsilon_0$  is the vacuum permittivity (electric constant),  $\mu_0$  is the vacuum permeability (magnetic constant) and  $\frac{1}{c^2} = \epsilon_0 \mu_0$ , with  $c$  being the speed of light in vacuum, the operator  $\nabla$ , is known as Nabla operator and in Cartesian coordinates, is defined as:

$$\nabla = \left( \frac{\partial}{\partial x}, \frac{\partial}{\partial y}, \frac{\partial}{\partial z} \right). \quad (2.5)$$

By applying the rotational operator to equation (2.3), it can be rewritten as,

$$\nabla \times (\nabla \times \mathbf{E}) = -\frac{\partial}{\partial t} [\nabla \times \mathbf{B}], \quad (2.6)$$

and, afterward, by replacing the second term of the above equation with equation (2.4), it results in the following equation,

$$\nabla \times (\nabla \times \mathbf{E}) = -\frac{1}{c^2} \frac{\partial^2 \mathbf{E}}{\partial t^2}, \quad (2.7)$$

lastly, replacing the vectorial identity  $\nabla \times (\nabla \times \mathbf{E}) = \nabla(\nabla \cdot \mathbf{E}) - \nabla^2 \mathbf{E}$  in the equation (2.7), and since we know that  $\nabla \cdot \mathbf{E}$  is zero, from equation (2.1), the following linear wave equation is derived

$$\nabla^2 \mathbf{E} - \frac{1}{c^2} \frac{\partial^2 \mathbf{E}}{\partial t^2} = 0. \quad (2.8)$$

We identify this equation as describing the propagation of the electric field  $\mathbf{E}$  in both space and time. To find a solution, we consider a harmonic wave-like solution that travels with angular frequency  $\omega$ , characterized by the phase factor  $e^{-i\omega t}$ . Thus, we propose a solution in the form [10]:

$$\mathbf{U}(\mathbf{r}, t) = \mathbf{U}(\mathbf{r})e^{-i\omega t}. \quad (2.9)$$

Substituting this proposed solution (2.9) into the wave equation (2.8) and simplifying, we arrive at the Helmholtz equation, given by [11]:

$$(\nabla^2 + k^2)\mathbf{U}(\mathbf{r}) = 0. \quad (2.10)$$

with  $k = \frac{\omega}{c}$  being the wave number. In the above derivation, it is assumed that the sources or losses are known, and since we are studying beams which propagate in air and are monochromatic, these assumptions are still valid. If we assume that the variation in  $x$  and  $y$  directions are larger compared to the variation in the  $z$  direction, we can simplify the Helmholtz equation (2.10) by neglecting the second derivative with respect to  $z$ , denoted as  $\frac{\partial^2}{\partial z^2}$  leading to the approximation:

$$\left| \frac{\partial^2 U}{\partial z^2} \right| \ll \left| 2k \frac{\partial U}{\partial z} \right|. \quad (2.11)$$

This approximation is known as the paraxial wave approximation, which implies that the beam propagates without significant divergence from the beam axis. Under this assumption, the Helmholtz equation simplifies to what is termed as the paraxial Helmholtz equation

$$\nabla_T^2 U - 2ik \frac{\partial U}{\partial z} = 0, \quad (2.12)$$

where  $\nabla_T^2 = \frac{\partial^2 U}{\partial x^2} + \frac{\partial^2 U}{\partial y^2}$  is the transverse Laplacian operator.

In summary, ignoring the less significant terms, what we are left with is a more focused equation that describes the behavior of paraxial waves specifically. Adjusting the boundary conditions, we can identify several solutions to this equation, focusing particularly on the most significant ones for this study in the subsequent sections.

## 2.2 Structured light beams

This section delves into the characterization of different types of optical beams, starting with the fundamental solutions such as the Gaussian beams, and then extending to more complex structured beams such as H-G, L-G, and B-G beams. By examining these beam types, we can uncover how their distinct intensity profiles and phase distributions influence their exploration in various optical applications.

### 2.2.1 Gaussian beams

As we know the paraxial Helmholtz equation can be solved in different coordinate systems. Since the OAM of optical beams is a propriety related with cylindrical symmetry patterns, it is convenient to rewrite the paraxial Helmholtz equation in cylindrical coordinates,

$$\frac{\partial^2 u}{\partial \rho^2} + \frac{1}{\rho} \frac{\partial u}{\partial \rho} + \frac{1}{\rho} \frac{\partial^2 u}{\partial \phi^2} - 2ik \frac{\partial u}{\partial z} = 0, \quad (2.13)$$

with  $\rho$  representing the axial radius,  $z$  is the propagation axis and  $\phi$  the polar angle. In this form, equation (2.13) can be written independently of  $\phi$ , and, therefore vanishing the third term in the above equation,

$$\frac{\partial^2 u}{\partial \rho^2} + \frac{1}{\rho} \frac{\partial u}{\partial \rho} - 2ik \frac{\partial u}{\partial z} = 0. \quad (2.14)$$

A widely known solution to the paraxial Helmholtz equation is a spherical wave given by [12]

$$U(r) = \frac{U_0}{r} \exp(-ikr), \quad (2.15)$$

where  $U_0$  is the wave amplitude and  $r$  the distance from the source, we can confirm that the equation (2.15) satisfies both equation (2.10) and (2.12) due to its small variation across distance comparable to its wavelength. When we replace  $z$  in equation (2.15) by  $g(z) = z - \xi$ , where  $\xi$  represents a simple shift in position, and represent the same wave but centered in  $z = \xi$ . It remains a solution of the Helmholtz equation even if  $\xi$  is complex. In this case, the solution acquires very different properties and in the case that  $\xi$  is a pure imaginary, we get the complex envelope of the Gaussian beam,



$$U(\rho, z) = \frac{U_0}{g(z)} \exp\left(ik \frac{\rho^2}{2g(z)}\right), \quad (2.16)$$

where  $g(z) = z + iz_0$ . Using two defined real functions  $R(z)$  and  $w(z)$  to write the phase and amplitude of the previous envelope.

$$\frac{1}{g(z)} = \frac{1}{R(z)} - \frac{i\lambda}{\pi w^2(z)} \quad (2.17)$$

By applying this approach, the complete complex envelope of the Gaussian beam is given by

$$U_G(\rho, z) = U_0 \frac{w_0}{w(z)} \exp\left[-\frac{\rho^2}{w^2(z)}\right] \exp\left[-ikz - ik \frac{\rho^2}{2R^2(z)} + i\zeta(z)\right]. \quad (2.18)$$

where the beam parameters, describe the Gaussian beam's waist  $w_0$  that denotes the minimum diameter where the beam intensity is highest, radius  $w(z)$  describing how the width of the beam changes as it propagates, Rayleigh range  $z_0$  specifying the distance over which the beam remains approximately collimated before diverging, and the wavefront curvature  $R(z)$  that varies along the propagation direction  $z$ , influencing how the beam's phase changes as illustrated in Figure 2-1, they are given by

$$w(z) = w_0 \sqrt{1 + \left(\frac{z}{z_R}\right)^2}, \quad R(z) = z \left[1 + \left(\frac{z_R}{z}\right)^2\right], \quad \zeta(z) = \tan^{-1}\left(\frac{z}{z_R}\right), \quad w_0 = \sqrt{\frac{\lambda z_R}{\pi}}. \quad (2.19)$$

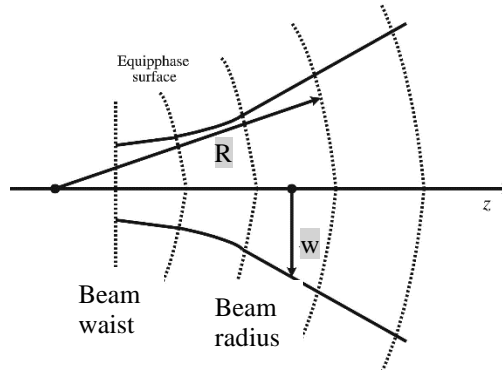


Figure 2-1 Schematic diagram of Gaussian beam propagation [13].

The Gaussian beam is renowned for its distinctive characteristics crucial in optics, notably its wavefront curvature during propagation along the  $z$ -axis. Initially near its focal point ( $z \approx 0$ ), the Gaussian beam exhibits a nearly planar wavefront due to its highly curved initial phase profile, as depicted in Figure 2-1. As  $z$  increases, the wavefront curvature becomes more pronounced, transitioning from nearly flat to a spherical shape, with the radius of curvature  $R(z)$  approaching  $z$ . This evolution is pivotal in various optical applications. In experimental setups employing SLMs, modifying the phase of incident Gaussian beams plays a pivotal role in generating diverse beams such as L-G, H-G, and B-G beams.

### 2.2.2 Laguerre-Gaussian beams:

As said previously, the Gaussian beam is not the only beam-like solution of the paraxial Helmholtz equation (2.12). There are solutions that have non-Gaussian intensity distributions but share the same wavefronts as gaussian beams, this means they have the same curvature of wavefronts as gaussian beams. One such notable solution is the L-G beams which are solutions to the paraxial Helmholtz equation in cylindrical coordinates. These beams are characterized by their concentric ring-like intensity distributions and are described by a Gaussian envelope and the Laguerre polynomial.

$$LG_{lm}(\rho, \varphi, z) = A_{lm} \frac{w_0}{w(z)} \left( \frac{\rho}{w(z)} \right)^l L_m^l \left( 2 \frac{\rho^2}{w^2(z)} \right) \exp \left[ -\frac{\rho^2}{w^2(z)} \right] \times \exp \left[ -ikz - ik \frac{\rho^2}{2R(z)} \mp il\varphi + i(l + 2m + 1)\zeta(z) \right], \quad (2.20)$$

with  $L_m^l$  representing the generalized Laguerre polynomials, where the integers  $l = 0, 1, 2, \dots$  and  $m = 0, 1, 2, \dots$  are azimuthal and radial indices, respectively. The intensity profile of a L-G beam exhibits a vortex structure at the center, where the intensity is zero, and the phase winds around the axis of propagation [12]. The functions  $w(z)$ ,  $R(z)$ ,  $\zeta(z)$ , and  $\omega_0$  are as previously defined by equation (2.19).

### 2.2.3 Hermite-Gaussian beams:

On the other hand, H-G beams provide a different class of solutions to the paraxial Helmholtz equation, in the Cartesian coordinate system. These beams exhibit a petaloid or lobe-like intensity structure, with multiple lobes in their intensity profile depending on the indices  $l$  and  $m$ . Although they have a more complex intensity distribution compared to L-G beams, H-G beams share a common feature with Gaussian beams: their wavefronts have the same curvature, which means they can be described by a similar Gaussian function in terms of the wavefront curvature. These types of beams are described by their characteristic intensity distribution, given by:

$$HG_{lm}(x, y, z) = A_{lm} \frac{w_0}{w(z)} G_l \left[ \frac{\sqrt{2}x}{w(z)} \right] G_m \left[ \frac{\sqrt{2}y}{w(z)} \right] \times \exp \left[ -ikz - ik \frac{x^2 + y^2}{2R(z)} + i(l + m + 1)\zeta(z) \right], \quad (2.21)$$

where

$$G_l(u) = H_l(u) \exp \left( -\frac{u^2}{2} \right), \text{ with } l = 0, 1, 2, \dots \quad (2.22)$$

The  $G_l(u)$  denotes the Hermite-Gaussian function of order  $l$  and  $A_{l,m}$  constant, with  $H_l$  being the Hermite polynomials. The fundamental L-G beam  $LG_{00}$ , akin to the lowest-order H-G beam  $HG_{00}$ , corresponds to the simple Gaussian beam.

## 2.2.4 Bessel-Gaussian beams:

Bessel beams are non-diffracted beams, which are special solution of Helmholtz equation in cylindrical coordinates [7], they exhibit self-healing properties, meaning they can reconstruct after encountering an obstacle. This is due to the re-interference of unblocked light behind the obstacle. While ideal Bessel beams cannot exist due to their infinitely extended light field structure, Bessel-Gaussian beams serve as practical approximations. These beams maintain non-diffracting characteristics over finite distances. The complex amplitude of an  $l$ -order B-G beam is [7]:

$$BG_p(r, \phi, z) = A_p J_p(k_r r) \exp \left[ i k_z z + i p \phi - \frac{r^2}{w_0^2} \right], \quad (2.23)$$

where  $A_p$  is a normalization constant,  $J_p$  is the Bessel function of the first kind and order  $p$ ,  $k_r$  represents the wave number associated with the radial direction, describing how the spatial frequency of the wave varies with distance from the beam  $r$ -axis.  $k_z$  on the other hand, denotes the wave number in the direction of propagation along the  $z$ -axis, determining how the phase of the wave evolves as it travels through space. In simpler terms, these conditions ensure that the wave has planar wavefronts, meaning the wavefronts are flat and parallel to the  $z$ -axis, and the rays of the wave are also parallel to the  $z$ -axis.

B-G beams can be generated in various ways, including the overlap of L-G modes. For the fundamental mode ( $p = 0$ ), a Gaussian beam is combined with a L-G mode with azimuthal number  $l = 0$ , resulting in a B-G beam with a maximum central intensity and a ring-like structure around it. For higher-order modes, where  $l > 0$  and  $p > 0$ , the overlap of a Gaussian envelope with the phase distribution of the L-G mode generates higher-order B-G beams characterized by a central ring and additional annular structures around it. In Figure 2-2, intensity profiles of different types of optical beams are presented. The Gaussian beam (a) exhibits a centralized intensity profile, with maximum intensity at the beam center, gradually decreasing towards the edges following a Gaussian distribution. For the H-G beam in modes  $l = 1, m = 1$  (b), lobed intensity patterns are visible along the beam. The L-G beam in modes  $l = 1, m = 1$  (c) displays a central intensity ring, typical of beams carrying OAM. In addition to the main ring, a smaller secondary ring is observed, highlighting the helical phase structure of the beam around the optical axis. Lastly, the B-G beam in mode  $p = 1$  (d) also carries OAM. It shows concentric intensity rings around a central point.

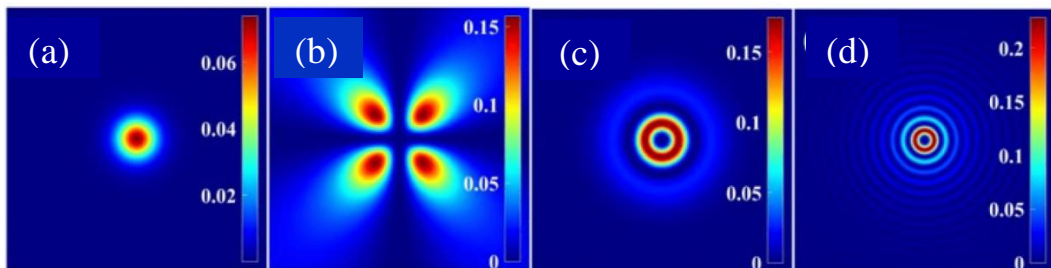


Figure 2-2 Transverse intensity distributions of typical structured light beams beyond the paraxial approximation. Shown from left to right are the cases of the fundamental Gaussian beam, the H -  $G_{11}$ , L -  $G_{11}$  and B -  $G_1$  beams, respectively [14].

## 2.3 Orbital Angular Momentum

As discussed in chapter 1, OAM is a fundamental property of light beams characterized by a helical phase front, causing the light to twist around its axis of propagation. OAM is quantized, meaning it can only take discrete values of  $\hbar l$ , where  $l$  is an integer and corresponds to a distinct mode or state of OAM, influencing the wavefront's phase distribution. This phase distribution includes a phase singularity along the axis of propagation, where the phase of the wavefront exhibits a  $2\pi$  ambiguity, leading to a doughnut-shaped intensity profile characteristic of OAM beams. Unlike H-G beams, which do not inherently carry OAM, L-G beams are known to carry OAM in orders where  $l_{LG} > 0$ . These beams exhibit a helical phase structure that results in a phase singularity along the propagation axis, forming a characteristic doughnut-shaped intensity profile. H-G beams can be combined with other beams to induce OAM [2]. Furthermore, B-G beams can also carry OAM in orders where  $p \neq 0$ . These beams combine a Gaussian envelope with the phase distribution of generalized Bessel functions, resulting in patterns of concentric rings with OAM characteristics.

When discussing OAM, we introduce a phase term  $e^{il\phi}$  in addition to the plane wave term,  $\phi$  represents the azimuthal angle around the propagation axis and  $l$  determines how many complete  $2\pi$  phase rotations the beam undergoes per wavelength. This helical symmetry around the propagation axis forms a corkscrew-like pattern in space, defining the spatial distribution of intensity and phase. As  $l$  increases, the size of the doughnut-shaped intensity profile expands, addition quantum unit of angular momentum per photon and the phase singularity along the propagation axis becomes more pronounced. The electric and magnetic fields of a light beam with OAM can be expressed as:

$$\mathbf{E}(\mathbf{r}, t) = E_0 \exp[i(kz - \omega t + l\phi)] \quad (2.24)$$

$$\mathbf{B}(\mathbf{r}, t) = B_0 \exp[i(kz - \omega t + l\phi)] \quad (2.25)$$

The presence of the  $e^{il\phi}$  term introduces a spatial phase variation around the propagation axis, giving rise to the twisted wavefront characteristic of OAM-carrying beams, as can be seen in equations (2.20) and (2.23) for L-G and B-G beams, respectively.

Angular momentum of light can be characterized through two fundamental quantities: angular momentum density ( $\mathbf{M}$ ) and total angular momentum ( $\mathbf{J}$ ). The momentum density is given by  $\mathbf{M} = \epsilon_0 \mathbf{r} \times (\mathbf{E} \times \mathbf{B})$ , signifies the direction and distribution of rotational momentum within the electromagnetic wave at each spatial point. It illustrates how angular momentum is spatially distributed throughout the wave. The total angular momentum, on the other hand, is given by  $\mathbf{J} = \epsilon_0 \int \mathbf{r} \times (\mathbf{E} \times \mathbf{B}) d\mathbf{r} = \mathbf{L} + \mathbf{S}$ , it encapsulates the cumulative angular momentum carried by the entire electromagnetic field. It incorporates contributions from both OAM SAM, providing a comprehensive measure of the overall angular momentum content of the electromagnetic wave.

An optical vortex exemplifies a field configuration where the intensity is zero along a central line, such as along the axis of a L-G beam for  $l \neq 0$ . This phenomenon is also referred to as a screw dislocation due to the corkscrew-like twist of the phase around the propagation axis. In a planar cross-section, this configuration appears as a phase singularity, a point where the electric field vanishes. In L-G beams, this azimuthal index  $l$  indicates the number of intensity

null lines or rings present in the standing wave pattern. This number also defines the OAM of the photons, where each unit increase in  $l$  represents an additional quantum of angular momentum carried by the photons.

There are various methods to induce spatial phase variation and generate beams carrying OAM. In our approach, we will use a SLM with a spiral phase mask. This technique can transform a Gaussian laser beam into a helical mode, where the wavefronts exhibit a corkscrew pattern with  $\theta$ -fold symmetry, represented by  $e^{i\theta}$ . This transformation introduces OAM into the beam, as previously explained in the context of beams carrying OAM.

In Chapter 3, we will extensively discuss this method and explore additional techniques. These methods provide flexible and efficient ways to control the properties of light beams, enabling the generation of structured light patterns.

## 2.4 Beam propagation

Beam propagation is a fundamental concept in optics that involves analyzing how light behaves as it travels through various media and interacts with different structures. This understanding is crucial for designing and simulating optical systems to achieve desired outcomes. In this section, we will delve into the mathematical frameworks used to describe light propagation, focusing on the Fresnel diffraction integral and its special case, the Fraunhofer diffraction approximation. We will also discuss the role of convolution and Fourier transformations in analyzing the behavior of light beams.

The study of beam propagation is grounded in the wave theory of light, significantly advanced by the works of Christiaan Huygens, Augustin-Jean Fresnel, and Joseph von Fraunhofer. Huygens' principle, formulated in the 17th century, posits that every point on a wavefront can be considered a source of secondary spherical wavelets. This principle is fundamental in understanding how light waves propagate, diffract, and interfere. In the early 19th century, Fresnel expanded on Huygens' principle by incorporating the concept of interference, leading to a more comprehensive wave theory of light. Fresnel's diffraction theory accounts for the phase changes and path differences of the secondary wavelets, providing a detailed description of near-field diffraction patterns. Joseph von Fraunhofer, also in the 19th century, simplified Fresnel's approach for far-field diffraction scenarios, where the wavefronts can be approximated as planar wavefront. This approximation led to the development of the Fraunhofer diffraction theory, which is easier to apply mathematically and is widely used in practical applications where the observation point is away from the diffracting object [16].

### 2.4.1 Fresnel diffraction integral

The Fresnel diffraction integral provides a comprehensive method for calculating the intensity distribution of light after it passes through apertures or encounters obstacles. This integral accounts for both the amplitude and phase changes of the light wave. The Fresnel diffraction integral is given by[17]:

$$U(x_2, y_2) = \frac{e^{ikz}}{i\lambda\Delta z} \int_{-\infty}^{\infty} \int_{-\infty}^{\infty} U(x_1, y_1) e^{i\frac{k}{2\Delta z}[(x_2-x_1)^2 + (y_2-y_1)^2]} dx_1 dy_1. \quad (2.26)$$

allows for calculating the intensity distribution at the observation plane  $(x_2, y_2)$  after light passes through apertures or encounters obstacles. Here,  $U(x_1, y_1)$  represents the wave's complex amplitude at the source plane coordinates  $(x_1, y_1)$ , and  $\Delta z$  the propagation distance over which diffraction is evaluated. The coordinates  $(x_2, y_2)$  are in the observation plane where the diffraction pattern is analyzed.

## 2.4.2 Fraunhofer diffraction

Fraunhofer diffraction is a valid approximation for situations where the distance between the light source and the observation plane is significantly larger than the dimensions of the diffracting structures. In this approximation, the quadratic phase term in the Fresnel integral is removed, simplifying it to a more tractable form [17]:

$$U(x_2, y_2) = \frac{e^{ikz} e^{i\frac{k}{2\Delta z}(x_2^2 + y_2^2)}}{i\lambda\Delta z} \int_{-\infty}^{\infty} \int_{-\infty}^{\infty} U(x_1, y_1) e^{-i\frac{k}{\Delta z}(x_1 x_2 + y_1 y_2)} dx_1 dy_1. \quad (2.37)$$

This allows for the direct evaluation of the intensity distribution at the observation plane through a Fourier transform. According to Goodman, “significantly larger” is defined by the inequality:

$$\Delta z > \frac{2D^2}{\lambda} \quad (2.28)$$

In many cases, the integral of Fresnel, which describes the propagation of light through a lens or aperture, can be expressed in terms of convolution. This mathematical approach leverages the properties of Fourier transforms, simplifying the solution by treating the integral as a straightforward multiplication in Fourier space. This technique is particularly useful for quickly calculating the diffraction pattern of light when faced with complex optical configurations. In the context of beam propagation simulation, convolution is often used to calculate the intensity distribution of light at the observation plane, taking diffraction into account.

$$C_{fg}(x) = f(x) \otimes g(x) = \int_{-\infty}^{\infty} f(x')g(x - x')dx' \quad (2.29)$$

$f(x)$  represents the initial complex amplitude distribution of the light wave at the aperture or obstacle. This function encapsulates the spatial structure and phase of the wavefront before encountering diffraction effects.  $g(x)$  signifies the impulse response or point spread function associated with the aperture or obstacle. It characterizes how the light wave changes as it propagates through or diffracts around the optical element.

## CHAPTER 3

# Structured light manipulation: an overview

In this chapter, we provide an overview of advanced techniques for manipulating structured light, with a primary focus on free-space methods using Spatial Light Modulators (SLMs). We will also describe other techniques for structured light generation, exploring both free-space and fiber-optic methodologies. Our goal is to understand how these techniques can be used for precise control and generation of structured light beams.

### 3.1 In fibers

Light manipulation in fiber optics involves sophisticated techniques that utilize the structural and material properties of optical fibers to achieve specific mode excitation in the cladding or core modes. Optical fibers provide a versatile platform for light manipulation due to their compact structure and controllable properties. This section covers two main approaches for light manipulation in optical fibers: Long-Period Fiber Gratings (LPFGs) and Chiral Long-Period Fiber Gratings (CLPFGs).

#### 3.1.1 Long-Period Fiber Grating

LPFGs are optical devices that introduce a periodic variation in the refractive index along the core of an optical fiber. This periodicity is characterized by the grating period  $\Lambda$ , which can be adjusted to enable efficient coupling between the fiber's fundamental mode,  $LP_{01}$ , and other core mode or a specific cladding mode  $LP_{0m}$  [18]. The phase matching condition for coupling between the fundamental mode and a cladding mode is given by,

$$\beta_{core} - \beta_{clad,m} = \frac{2\pi m}{\Lambda} \quad (3.1)$$

where  $\beta_{core}$  is the propagation constant of the fundamental mode  $LP_{01}$ ,  $\beta_{clad,m}$  is the propagation constant of the  $m$ -th cladding mode ( $LP_{0m}$ ), and  $m$  is the mode order.

LPFGs can be used for the generation of beams with OAM by properly exciting a combination of  $LP_{0m}$  modes using a mode converter [19]. Initially, a Gaussian beam in the  $LP_{01}$  mode from a single-mode fiber is coupled into a multi-mode fiber where it is transformed into a higher-order mode, such as  $LP_{11}$ , via an LPFG as shown in Figure 3-1. This  $LP_{11}$  mode can be expressed as a superposition of two degenerate modes,  $LP_{11a}$  and  $LP_{11b}$ , with a phase difference of  $\pm \frac{\pi}{2}$  introduced by birefringence induced by two metal plates that mechanically press the fiber illustrated by the flat slab in Figure 3-1. The resulting beam exhibits OAM, where the OAM is determined by the combination of these modes:

$$OAM_{\pm l} = LP_{lma} \pm i \times LP_{lmb}, \quad (3.2)$$

where the  $LP_{lma}$  and  $LP_{lmb}$  denote the two degenerate modes of the  $LP_{lm}$  mode with a phase difference of  $\pm \frac{\pi}{2}$ .



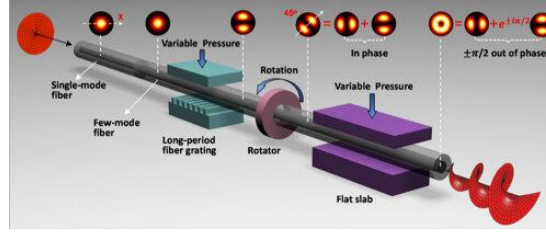


Figure 3-1 Principle of the controllable all-fiber OAM beam converter [19].

### 3.1.2 Chiral-Long-Period Fiber Grating

CLPFGs structures feature a helical modulation in the refractive index along the fiber, enabling direct excitation of OAM modes without the need for additional complex equipment. CLPFGs are typically fabricated by introducing a helical structure into the optical fiber during manufacturing [20], traditionally achieved by twisting a section of fused fiber. The resulting modulation in the refractive index creates a periodic arrangement that efficiently couples light into OAM modes. Recent technological advancements have facilitated the fabrication of ultra-short CLPFGs using CO<sub>2</sub> lasers to inscribe helical curves on the fiber surface. This approach provides greater control over the grating modulation parameters, enhancing coupling efficiency for higher-order OAM modes, as reported in studies demonstrating the excitation of OAM modes with coupling efficiencies of 95% and 98%, respectively, in grating lengths of 4.75 cm, with  $l = 2$  and 3 [21].

## 3.2 In free space

Structured light manipulation in free space involves the use of various optical and electro-optical devices to precisely control the phase, amplitude, and polarization of light beams. By tailoring the properties of light beams in free space, it is possible to achieve sophisticated beam shapes and modes, such as optical vortices and beams carrying OAM. The primary techniques and devices used for free space structured light manipulation include axicons, cylindrical lenses, spiral phase plates, holographic gratings, metamaterials, Q-plates and SLMs.

### 3.2.1 Optical elements

Optical elements are essential components that allow for the wavefront shaping by introducing spatial phase difference across the profile of the optical beam. In this regard they allow precise control over the light beam's phase, intensity, and polarization, enabling the generation and modulation of complex light structures. Below are some of the key optical elements used in free space structured light manipulation.



### 3.2.1.1 Axicons

Axicons are conical-shaped optical components known for their ability to focus incident light into a ring-shaped intensity distribution rather than a conventional focal spot. This unique property arises from the gradual change in the phase of light as it propagates through the axicon's surface [22]. As light passes through an axicon, it undergoes a continuous phase shift, resulting in both constructive and destructive interference patterns in the focal plane. The conical geometry of the axicon, defined by parameters such as the base angle  $\gamma$  and radial coordinate  $\rho$ , facilitates this phase modulation, as illustrated in Figure 3-2. By illuminating the axicon with a Gaussian beam, the incident light's phase is altered radially, generating an annular intensity pattern. This ring-shaped distribution is characteristic of Bessel beams produced by axicons, which exhibit non-diffracting properties and an extended depth of focus.

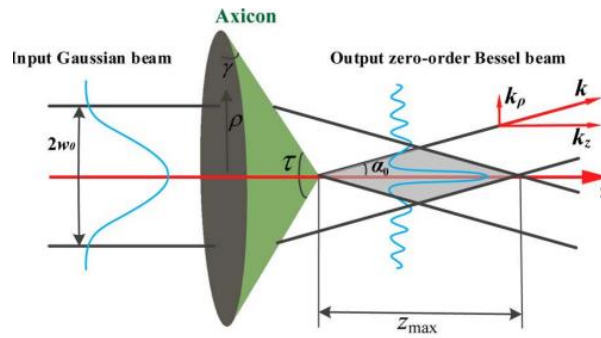


Figure 3-2- Schematic diagram for zero-order Bessel generation by Axicon, where  $\gamma$  is the base angle of the axicon [22]

### 3.2.1.2 Cylindrical lenses

Cylindrical lenses play a pivotal role in mode conversion by introducing astigmatism into a light beam. Astigmatism occurs when a cylindrical lens alters the beam's curvature along one axis while leaving the perpendicular axis unchanged. This manipulation induces a spatially varying Gouy phase across the beam profile, essential for transforming H-G modes into L-G modes [23]. To illustrate this concept, consider Figure 3-3, which shows a cylindrical lens mode converter designed to convert a H-G  $x = 1, y = 0$  mode into a corresponding L-G mode with  $l = 1$  and  $p = 0$ . Positioned at a separation of  $\frac{f}{\sqrt{2}}$ , where  $f$  is the focal length, the cylindrical lenses are aligned to match the astigmatic properties of the beam. This configuration ensures that the requisite phase difference for mode conversion is achieved. In practice, cylindrical lenses are engineered to achieve a specific phase difference between different components of the beam, critical for facilitating H-G to L-G mode conversion.

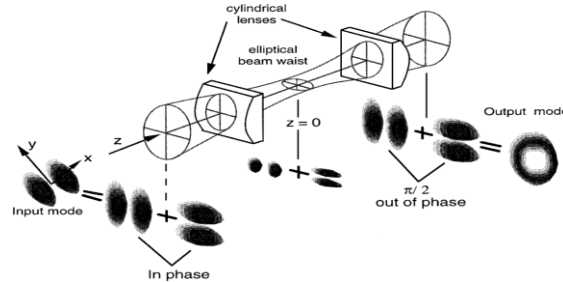


Figure 3-3 – The cylindrical lens mode converter for the conversion of a H-G  $x = 1, y = 0$  mode into the corresponding L-G mode with  $l = 1$  and  $p = 0$ . The lenses of focal length  $f$  are separated by  $\frac{f}{\sqrt{2}}$  [24].

### 3.2.1.3 Spiral phase plates

Another way to implement the vortex beam is the spiral phase plate (SPP) that functions as an optical component that introduces an azimuth-dependent phase delay in an incident optical field [25]. Typically, it appears as a transparent plate with a height profile that increases proportionally with the azimuthal angle, as depicted in Figure 3-4. The step height  $h$  of the SPP is described by the relation

$$h = \frac{h_s \theta}{2\pi} + h_0, \quad (3.3)$$

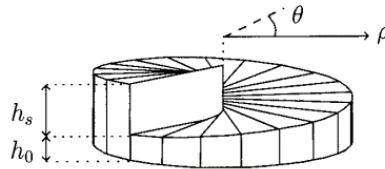


Figure 3-4 Sketch of the spiral phase plate. The top surface spirals upward from height  $h_0$  to  $h_0 + h_s$  [25].

where  $h_s$  represents the step height and  $h_0$  denotes the base height of the plate. This configuration results in an azimuth-dependent phase modulation given by

$$\phi(\theta, \lambda) = \frac{2\pi}{\lambda} \left[ \frac{(n - n_0)h_s \theta}{2\pi} + nh_0 \right], \quad (3.4)$$

where  $n$  and  $n_0$  denote the refractive indices of the SPP material and the surrounding medium, respectively. When a Gaussian beam passes through the SPP, it undergoes a spatial phase shift across its profile, transforming it into a helical beam with a topological charge  $Q = \frac{h_s(n - n_0)}{\lambda}$ , thereby imparting OAM to the beam.

### 3.2.2 Q-Plates

Q-plates are advanced optical components based on liquid crystal (LC) technology designed to manipulate the polarization and phase of light. These devices utilize a specific azimuthal pattern in the LC director to impart spatially varying phase shifts, which allows them to perform a variety of optical functions, including the generation of beams with OAM. Q-plates are significant in the field of structured light for their ability to control both the polarization state and the spatial structure of light beams. A Q-plate consists of a thin layer of LC material sandwiched between two glass plates. The orientation of the LC director within the plate follows a specific azimuthal pattern described by the topological charge  $l$ , which can be an integer or half-integer. The angle  $\alpha$  between the LC director and a reference axis is given by:

$$\alpha(\phi) = l\phi + \alpha_0, \quad (3.5)$$

where,  $\phi$  denotes the azimuthal angle in the plane of the Q-plate and  $\alpha_0$  is the initial angle of the director. When circularly polarized light interacts with a Q-plate, the azimuthal pattern of the LC director induces a spatially varying phase shift:

$$\delta(\phi) = 2l\phi. \quad (3.6)$$

This phase shift creates a helical wavefront in the transmitted light, which is characterized by the OAM (see Figure 3-5). The relationship between the input polarization state and the generated OAM can be described as follows:

$$|LCP\rangle \rightarrow |RCP\rangle e^{i2l\phi}, |RCP\rangle \rightarrow |LCP\rangle e^{-i2l\phi} \quad (3.7)$$

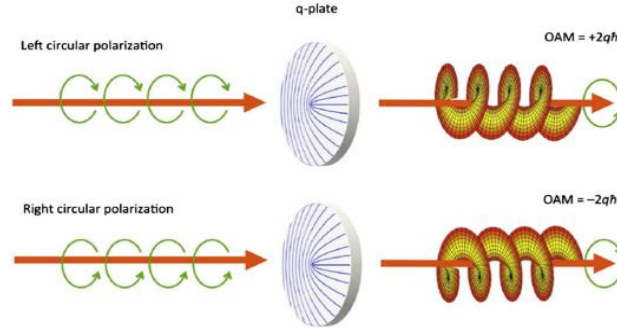


Figure 3-5 - Q-plate working principle: a pictorial representation of equation (3.6) in the optimal case  $\Delta = \pi$  [26].

Q-plates offer high conversion efficiency (over 97% [27]), compactness, stability, wide frequency range operation, and electrical control for wavelength adjustment. They also enable superposition of SAM and OAM states without interferometric setups. However, Q-plates have limitations: they are not suitable for all spectral ranges, are sensitive to temperature and environmental fluctuations, require high-precision fabrication, may suffer from optical losses, and cannot handle very high light intensities.

### 3.3 Spatial Light Modulators

The most common method for generating structured light is through the use of a SLM in free space. This device allows for the control of the phase or amplitude of the optical beam based on the electric field applied to each of its pixels [28]. By doing so, it is possible to alter the wavefront of the incident beam, generating beams with specific properties, such as OAM. Essentially, the SLM shapes the wavefront of the incident beam by modulating the refractive index of its display. Usually, to achieve the desired result, it is assumed that the incident beam on the SLM screen is a Gaussian beam. Then, appropriate phase masks are then employed to modulate the wavefront accordingly.

#### 3.3.1 Structure and operation principles

Among the various SLM technologies, there are two main types distinguished by their operational mechanisms: Micro-Electro-Mechanical Systems (MEMS)-based SLMs and Liquid Crystal on Silicon (LCoS)-based SLMs. MEMS-based SLMs employ micromechanical structures, such as tilting mirrors, to modulate light. These devices are known for their ability to handle high light intensities and achieve high modulation rates, making them ideal for high-definition displays and adaptive optics applications. MEMS SLMs are characterized by their

robustness and high optical throughput, which are advantageous for dynamic and high-resolution imaging tasks [29].

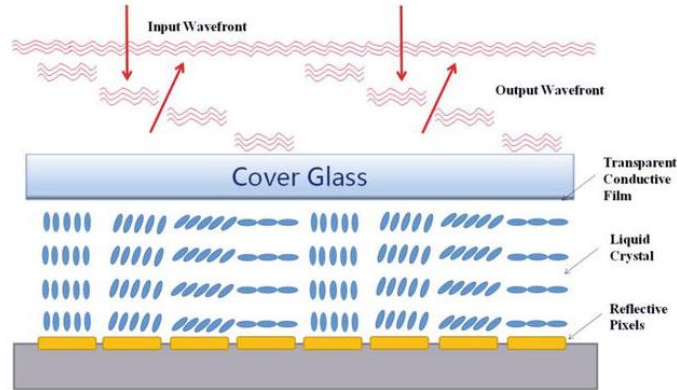


Figure 3-6 Typical structure of a reflective LC-SLM [30].

In contrast, LCoS SLMs, such as the Pluto Phase Only SLM, use a liquid crystal layer aligned parallel to a glass substrate and a CMOS (Complementary Metal-Oxide-Semiconductor) silicon backing. When no electric field is applied, the liquid crystal molecules are oriented at 90 degrees relative to a vertical axis, forming a matrix of pixels. The CMOS circuitry beneath this matrix allows for the electrical control of the phase delay across each individual pixel to achieve the desired wavefront modulation, as illustrated in Figure 3-6. This technology exploits the birefringent properties, a phenomenon where a single incident light ray splits into two rays with different refractive indices and propagation directions. These rays are known as the ordinary and the extraordinary ray. The ordinary ray follows the standard laws of refraction, while the extraordinary ray's path depends on the birefringent material's optical axis and the direction of light propagation. For a non-zero birefringence in the liquid crystal material, the difference  $\Delta n$  between the ordinary refractive index  $n_o$  and the extraordinary refractive index  $n_e$ , as Figure 3-7 illustrate, allows for the creation of a spatially varying phase delay, that is, at each pixel of the SLM given by

$$\Delta n = n_e - n_o > 0 \quad (3.8)$$

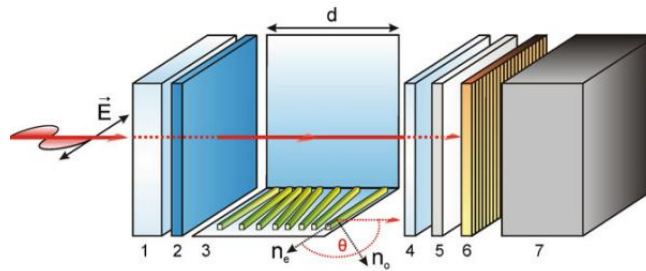


Figure 3-7 The structure of a single cell is shown at an expanded scale [31].

By applying varying voltages to the pixelated electrodes, LCoS SLMs control the orientation of the liquid crystal molecules. This orientation change alters the refractive index of the medium and introduces a spatially varying phase shift to the incident light. The applied electric field enables precise phase delay modulation across the SLM, which allows for the creation of complex optical patterns. The phase delay  $\Delta\phi$  introduced by a single pixel of the SLM can be expressed as:

$$\Delta\phi = \frac{2\pi(\Delta n)l}{\lambda} \quad (3.9)$$

where  $l$  is the thickness of the liquid crystal layer and  $\lambda$  is the wavelength of the incident light. By adjusting the voltage on each pixel, the device can achieve a phase delay ranging from 0 to  $2\pi$  or more, depending on the SLM, with a typical resolution of up to 256 discrete levels. The active area of the SLM generally contains between 1000 and 2000 pixels, with a pixel pitch of approximately  $10\ \mu m$ , and the reflectivity of these devices is usually above 80%, primarily limited by inherent medium losses and pixel gaps.

A crucial aspect of LCoS SLMs is their dependence on the polarization of the incident light. Liquid crystals exhibit birefringence, which causes the refractive index to vary based on the light's polarization direction. For optimal modulation, the incident beam must be linearly polarized, and its polarization state must align with the liquid crystal's optical axis, ensuring that the phase modulation introduced by the liquid crystal layer is maximized. Therefore, the polarization of the incident light is a key factor in determining the effectiveness of the phase modulation achieved by the SLM. By controlling the polarization, one can ensure that the phase retardation effect of the liquid crystal molecules is fully utilized, which is essential for obtaining consistent results in phase modulation and high-precision optical experiments.

### 3.3.2 Advantages and disadvantages

SLMs offer several advantages and some disadvantages, especially when compared to other techniques for structured light manipulation. They have high spatial resolution for fine control over the phase profile of the incident beam, surpassing fixed optical components such as axicons and cylindrical lenses, which lack flexibility in detailed manipulation. SLMs are versatile, allowing modulation of phase, amplitude, or polarization, making them suitable for a wide range of applications. This versatility contrasts with specialized devices like Q-plates, which focus primarily on manipulating polarization and phase. Another key advantage of SLMs is their real-time reconfigurability, which is essential for adaptive optics systems that dynamically correct optical aberrations to enhance imaging performance. Despite the SSPs having fixed phase profiles and lacking real-time adjustability, they offer a notable advantage with their high conversion efficiency, approaching nearly 100%. Their production is labor-intensive due to the challenge of smoothly achieving the required phase ramp, resulting in most commercially available SPPs being approximations of the ideal.

On the other hand, SLMs also present some limitations such as limited phase modulation range that may truncate phase profiles and reduce efficiency, and insufficient phase resolution for generating complex phase profiles required for high-quality OAM beams. They typically come with a factory-defined gamma curve, representing the non-linear relationship between input voltages and resulting phase shifts. This gamma curve may not always precisely match desired optical responses, potentially leading to inaccuracies in phase modulation. Users have the capability to adjust this curve to better align with the current response pattern of the SLM, thereby improving accuracy in practical applications. Moreover, SLMs are susceptible to optical losses and imperfections, particularly at pixel boundaries, which can degrade overall beam manipulation efficiency. Cost and complexity are also important considerations. High-quality SLMs are expensive and require precise calibration and maintenance for stable operation. Conversely, simpler optical components like axicons and cylindrical lenses are more cost-effective but lack the dynamic capabilities of SLMs.

## CHAPTER 4

# Experimental generation of structured light

In this chapter, we provide a detailed description of the experimental setup utilized for generating and analyzing structured light. The setup employs SLM to manipulate laser beams and produce distinct light patterns, H-G, L-G and B-G beams. Additionally, we discuss the GUI employed for controlling the experimental parameters. Finally, we present the outcomes and findings obtained from the experimental investigations.

### 4.1 Experimental Setup

The experimental setup is designed around several key components to achieve precise manipulation of structured light beams. Central to this setup is the Spatial Light Modulator (SLM), specifically the PLUTO-2.1 model for phase modulation. Accompanying the SLM is the Collimator (F810APC-1550). An Infrared Distributed Feedback Laser Diode (DFB) operating at 1554 nm with a power output of 7.5 dBm serves as the light source, providing stable and coherent illumination necessary for precise experimental conditions. The Laser Beam Profiler (LBP), BeamOn IR1550 model, plays a role in characterizing the spatial properties of the laser beam, ensuring alignment and verifying beam quality throughout the setup. The optical platform is further supported by a PBG51513 UltraLight Breadboard, offering a stable foundation for component mounting and alignment adjustments. Additional components include a Beam Splitter for directing light to different paths or instruments and Manual Polarization Controller with 3 paddles, enabling adjustments of light polarization as required, as seen in Figure 4.1 a) and b).

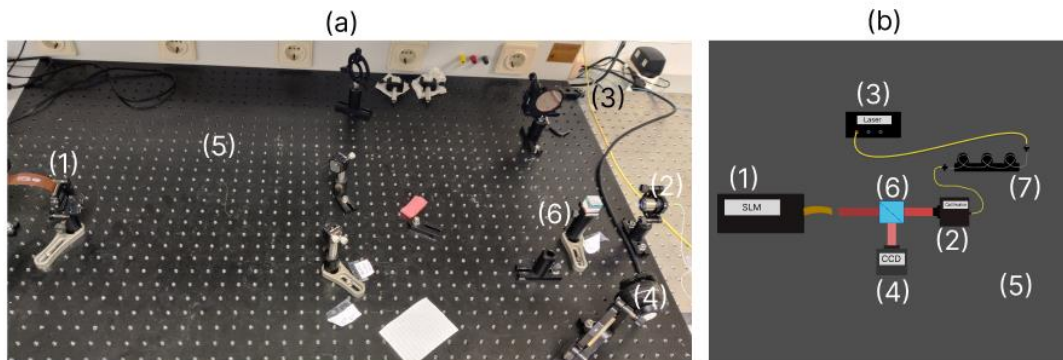


Figure 4-1 (a) Experimental set up used for manipulating light (b) Schema of the experimental set up. 1 - SLM, 2 - Collimator, 3- DFB, 4 - LBP, 5- Breadboard, 6- Beam splitter, 7 - Polarization controller

As we will use a SLM, consequently, it is necessary to employ phase masks, which represent a grayscale matrix depicting the variations in refractive indices within the SLM matrix, thereby causing the appropriate modulation of the wavefront. We will delve into more detail regarding the masks used to generate L-G beams and forked masks. The remaining H-G and B-G masks are derived from similar procedures.



### 4.1.1 Phase masks

To generate a phase mask corresponding to the L-G beams, our focus is on the phase component of the equation (2.20). The phase of a L-G beam consists primarily of the sum of its azimuthal phase  $e^{\pm l\phi}$  and radial phase  $\arg\left(L_m^l\left(\frac{2\rho^2}{\omega^2(z)}\right)\right)$ . For an SLM with width  $w$  and height  $h$  in pixels, using coordinates  $x \in \left[-\frac{w}{2}, \frac{w}{2}\right]$  e  $y \in \left[-\frac{h}{2}, \frac{h}{2}\right]$  centered at the middle of the SLM, the combined phase components yield the phase mask expressed as

$$\Phi_{L-G}(x, y) = \text{mod} \left[ l \cdot \arctan\left(\frac{y}{x}\right) + \arg\left(L_m^l\left(\frac{2(x^2 + y^2)}{\omega^2(z)}\right)\right), 2\pi \right]. \quad (4.1)$$

where *mod* normalizes the phase in the range  $[0, 2\pi]$  and denotes the modulo operator, and *arg* is the argument of a complex number. This phase mask is essential for manipulating the L-G beam's phase using an SLM. The analysis of equation (2.23) for B-G beams reveals insights into its phase components

$$\Phi_{B-G}(x, y) = \text{angle} \left[ J_p\left(\sqrt{x^2 + y^2}\right) \cdot \exp\left(-ip \cdot \arctan\left(\frac{y}{x}\right) + \pi\right) \right] + \pi. \quad (4.2)$$

Here,  $p$  denotes the mode of the B-G beam, and *angle* extracts the phase from the complex number. The addition of  $\pi$  ensures normalization of the phase within the range  $[0, 2\pi]$ .

In contrast, phase masks based on H-G beams are generated more simply due to the structure of Hermite polynomials. Each mode order  $xmode$  and  $y mode$  directly determines the pattern of divisions in the mask,

$$\Phi_{H-G}(x, y) = H_{xmode}(x)H_{ymode}(y). \quad (4.3)$$

On the other hand, forked diffraction gratings are known for their ability to separate beam components, specifically directing the modulated beam into the first order of diffraction while leaving the non-modulated beam in the zero order. To achieve this property, they combine the phase characteristics of the desired optical beam with a structured grating that features periodic divisions in both the  $x$  and  $y$  directions, as illustrated in figure 4.4a, which adjusts the position of the diffraction orders. Using this concept, by combining a phase mask such as a L-G mode with  $l = 3$ , with a linear phase ramp, given by equation (4.4), and then illuminating the resulting mask equation (4.5) with a Gaussian beam, the first-order diffracted beam emerges with OAM coupled to it, as shown in figure 4.4b.

$$gr(D_x, D_y) = \text{mod} \left[ 2\pi \left( \frac{1}{D_x}x + \frac{1}{D_y}y \right), 2\pi \right] \quad (4.4)$$

$$\Phi_{Forked}(x, y) = \text{mod} \left[ gr(D_x, D_y) + l \cdot \arctan\left(\frac{y}{x}\right), 2\pi \right] \quad (4.5)$$

This formulation combines the grating pattern with the azimuthal phase, enabling the creation of a forked phase mask tailored for beams with OAM. Our focus will be on leveraging these masks to enhance the performance on the generation of beams with OAM. Specifically, we will investigate the diffracted patterns observed in the first order of diffraction.

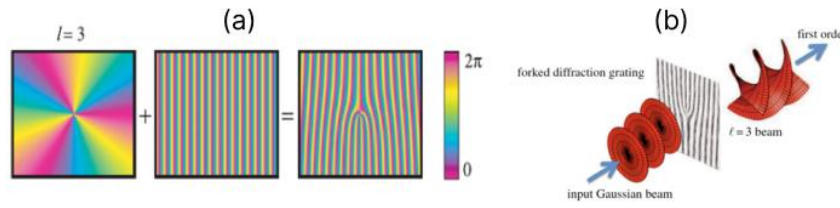


Figure 4-2 (a) - A combination of the phase distribution of the desired optical component (left) plus a linear phase ramp (middle) creates a forked diffraction grating (right), which can produce a helically phased beam. In this case  $l=3$  [32].  
(b) - When a standard laser beam illuminates a forked diffraction grating, the first-order diffracted beam has helical phase fronts [33].

## 4.2 Graphical User Interface

In order to enhance the intuitive and convenient manipulation of structured light, a graphical user interface (GUI) has been specifically developed. This chapter focuses on elucidating its primary functionalities while providing practical examples of the alignment and beam generation procedures.

### 4.2.1 Alignment and light modulation

The GUI should initially start on the alignment tab, as proper setup alignment is crucial to ensure effective wavefront modulation. If the setup is not aligned correctly, it will result in poor wavefront modulation. Alignment must be performed in both the horizontal and vertical directions. In the GUI should be selected the direction for alignment, as shown in the flow diagram in Figure 1. Immediately, a generated phase mask for alignment will be displayed. The user has the option to run the simulation and visualize the intensity profile. Parameters can always be adjusted, as illustrated in the screenshot of Figure 1 above the "Run Simulation" button. These simulations apply the Fraunhofer integral from equation (2.29), as explained earlier, along with convolutions in Fourier space, equation (2.30) to simulate propagation, ultimately extracting the intensity profile. Subsequently, the phase mask should be sent to the SLM, and the results captured by the LBP can be viewed on the right side of the tab. This process should be repeated for the other direction to achieve perfect setup alignment, allowing for proper beam modulation. The flow diagram in Figure 1 summarizes this alignment process.

In this alignment process, it is also important to consider polarization, as discussed in Chapter 3 regarding the SLM. For optimal modulation, the incident beam must be polarized to align with the liquid crystal's optical axis. This can be achieved using the manual polarization controller marked as (7) in Figure 4-1.

As illustrated in Figure 4-4, by varying the polarization state with horizontal and vertical alignment masks, the wave modulation can be observed from left to right. This observation indicates that the beam is correctly polarized on the right side.



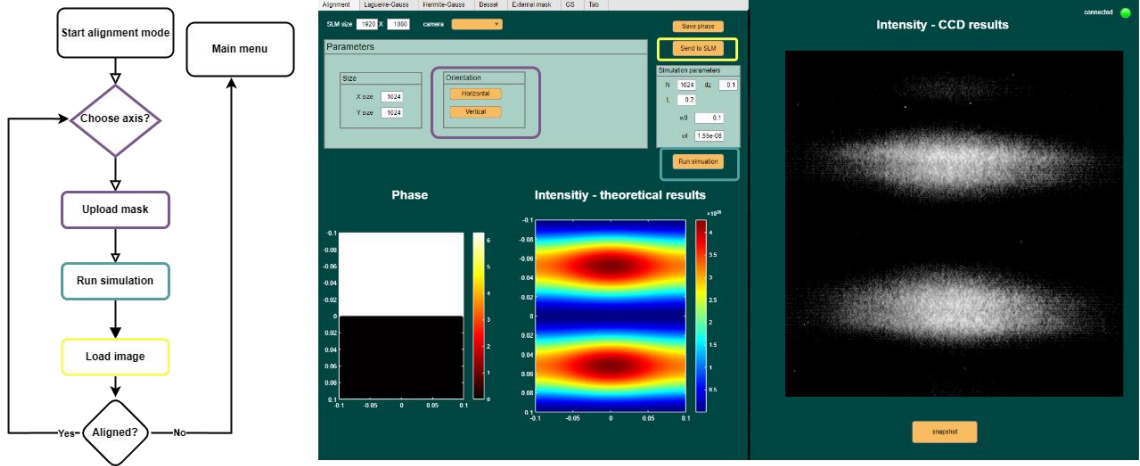


Figure 4-3 On the left, the functional flow diagram illustrates the alignment operation, detailing the sequential steps involved. On the right, a GUI screenshot highlights the alignment processes, providing a visual representation of the procedural steps

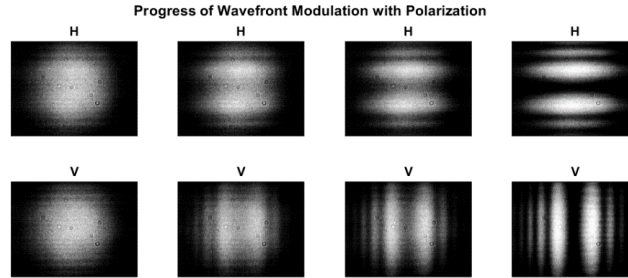


Figure 4-4 Progress of wavefront modulation with polarization variation for Horizontal (H) and Vertical (V) beam modulation.

Once alignment is successfully, structure light generation can begin. The layout for modulation follows a similar structure to the alignment layout, as shown in the screenshot in Figure 2. The tab interface allows for the selection of different beam types: L-G, H-G, and B-G. Users can then modify various parameters for mask generation, such as size, beam orders, radius, etc., as shown in the Figure 2 screenshot, with L-G used as an example. After defining the parameters, the desired beam mask, grating, or forked mask can be generated according to their matrix equation defined in equations from (4.1) to (4.5) representing the intensity levels on each pixel at the SLM matrix. Users can then simulate the intensity profile, send the mask to the SLM, visualize, and compare the results with the expected outcomes. If desired, users can save an image of the result. This process is similar for the other beam types and is illustrated in the flow diagram in Figure 2. For L-G, and B-G beams, additional parameters such as scale, angle, center, offset, and phase range can be adjusted. Additionally, for generating custom beam shapes, the External Masks tab allows users to upload their own phase mask designs. Once a mask is uploaded, it is previewed in the interface. The selected mask can then be applied to the SLM, and the process is similar to the other beams tabs. The source code of the GUI, including all the numerical routines used for generating the masks, communicating with the SLM, and running the simulations, can be found in the public repository at the reference link [34].

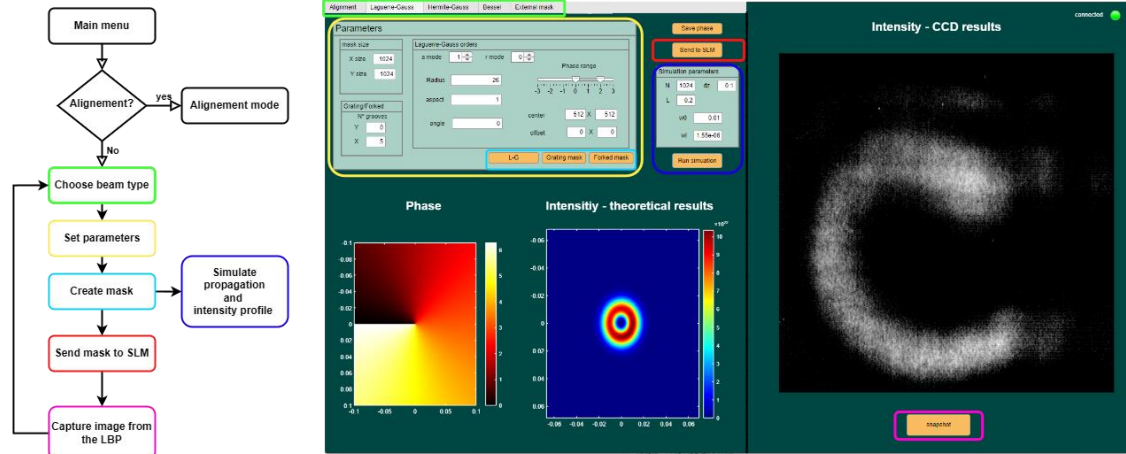


Figure 4-5 On the left, the functional flow diagram illustrates the main operations, detailing the sequential steps involved. On the right, a GUI screenshot highlights the important processes, providing a visual representation of the procedural steps.

## 4.3 Experimental results

The results were obtained for various beam types discussed in Chapter 2, including L-G, H-G and B-G beams. For each beam, we captured images of the phase masks (ranging from 0 to  $2\pi$ ), the simulated intensity profile, and the experimental intensity profile. Additionally, we conducted experiments using a forked diffraction phase mask to generate interference with unmodulated beam reflected on the surface of the SLM, demonstrating how the beam's characteristics change with increasing divisions in the grating (plotted on the horizontal axis). Finally, we present the various OAM modes recorded using this method.

### Hermite-Gaussian beams

Starting with H-G beams, the phase masks were used to modulate the beam structure, resulting in simulated intensities that closely matched the experimental measurements. The overall results were satisfactory; however, for some modes like (1,1) and (3,3), there was a noticeable repetition of intensity patterns, likely caused by interference effects. Despite these anomalies, the results for modes (2,0) and (2,1) were satisfactory and met the expected outcomes, demonstrating the effectiveness of phase masks in accurately shaping these beams.

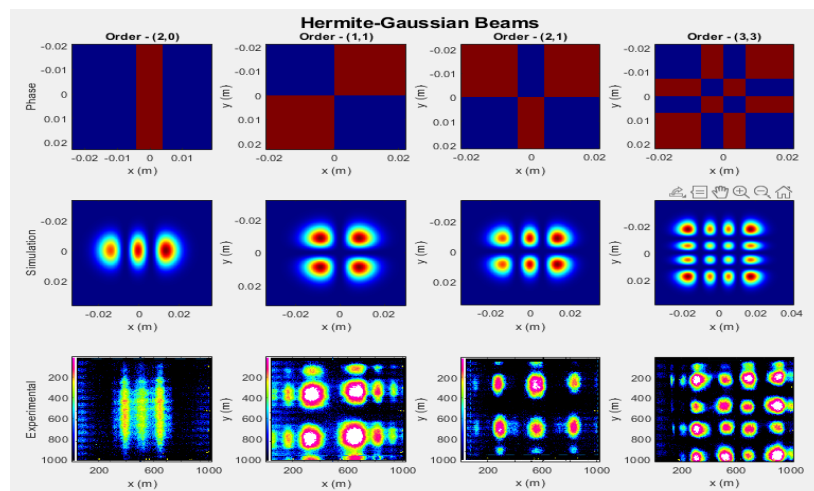


Figure 4-6 H-G beams results – First row shows the phase mask used, blue-0 and red- $2\pi$ , second row shows the results, and the third one gives the experimental results. H-G orders: (2,0), (1,1), (2,1), (3,3) from the left to the right.

## Laguerre-Gaussian beams

For the L-G beams, the experimental setup follows the same scheme: generating the phase mask, simulating the results, and comparing them with the experimental observations. However, there was a notable discrepancy between the experimental results and theoretical predictions. For instance, in the (1,1) mode, one would theoretically expect to observe a strong intensity ring characteristic of the topological charge  $l$  of OAM, surrounded by a less intense ring representing the radial index. However, the experimental results displayed an intensity ring beginning to form at 0 and gradually losing intensity as it rotates through  $2\pi$ . This pattern was consistently observed in higher modes such as (2,1) and (2,2) with  $l = 2$ , where the intensity ring exhibited a similar attenuation over each  $2\pi$  rotation. In contrast, the (0,1) mode performed as expected, showing a ring with a bright central spot, indicating that the issue lies specifically with the modulation of beams carrying OAM. This discrepancy suggests that there may be problems with the phase mask generation or alignment for higher-order modes, which affects the ability to accurately model and generate beams with the desired OAM properties. These issues highlight the importance of precise alignment and accurate phase modulation in achieving the correct beam profiles for OAM-carrying modes.

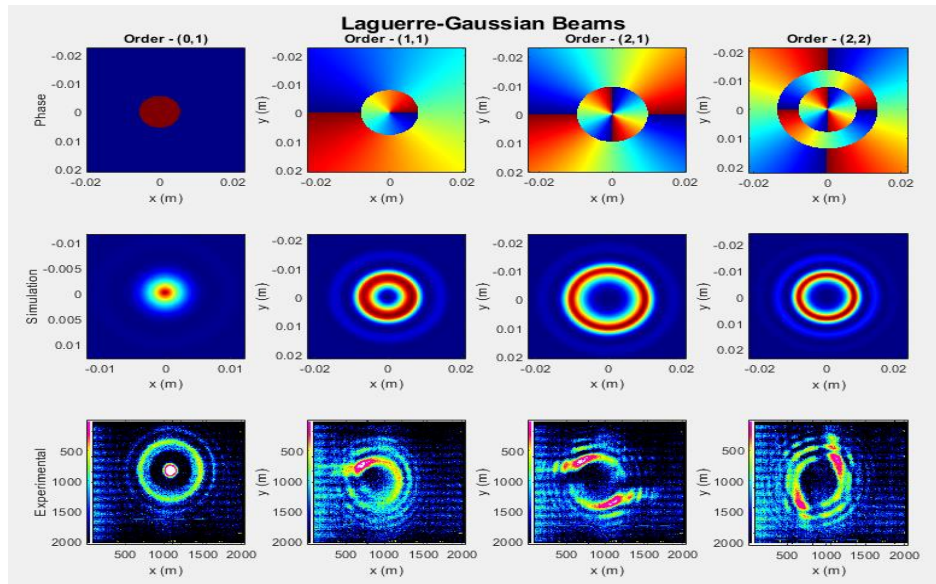


Figure 4-7 L-G beams results – First row shows the phase mask used, blue-0 and red- $2\pi$ , second row shows the results, and the third one gives the experimental results. L-G orders: (0,1), (1,1), (2,1), (2,2) from the left to the right.

## Bessel-Gaussian beams

In a parallel analysis to the L-G beams, similar challenges were encountered with B-G beams due to their shared characteristic of carrying OAM. The  $p = 0$  mode of B-G beams displayed the expected behavior, forming distinct rings across the screen. However, higher-order modes  $p = 1, 2, 3$  exhibited diminished intensity rings that did not align with theoretical predictions. This discrepancy highlights a consistent issue in the modulation process specifically related to OAM-carrying beams. The observed modulation patterns suggest potential inaccuracies in the phase masks used to impart OAM, exacerbated by alignment variations in the experimental setup.

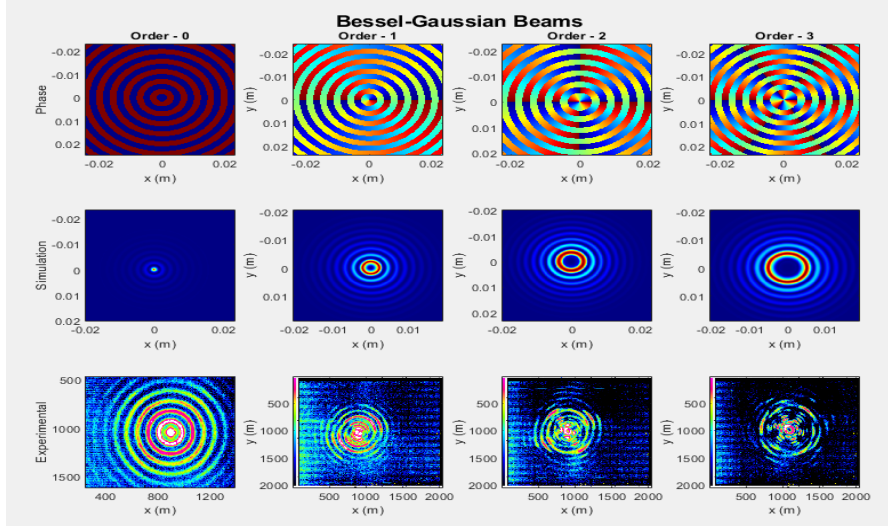


Figure 4-8 B-G beams results – First row shows the phase mask used, blue-0 and red- $2\pi$ , second row shows the results, and the third one gives the experimental results. B-G orders: 0, 1, 2, 3 from the left to the right.

## 4.4 Enhancing OAM generation

To improve the results obtained for OAM beams, we will proceed in two directions. The first will be to refine the parameters of the beam masks, and the second will be the application of forked phase masks.

### Geometric parameters optimization

Following the suboptimal outcomes observed for L-G and B-G modes with  $|l| > 0$ , we pursued a refined approach, by adjusting the scale, which is the radial scaling factor for the phase mask matrix. By fine-tuning this factor, we could effectively address the SLM's limitations such as pixel level and non-linear phase response, we present the outcomes structured similarly to previous sections, illustrating the enhanced purity of OAM carried by the L-G beams in Figure 4-9.

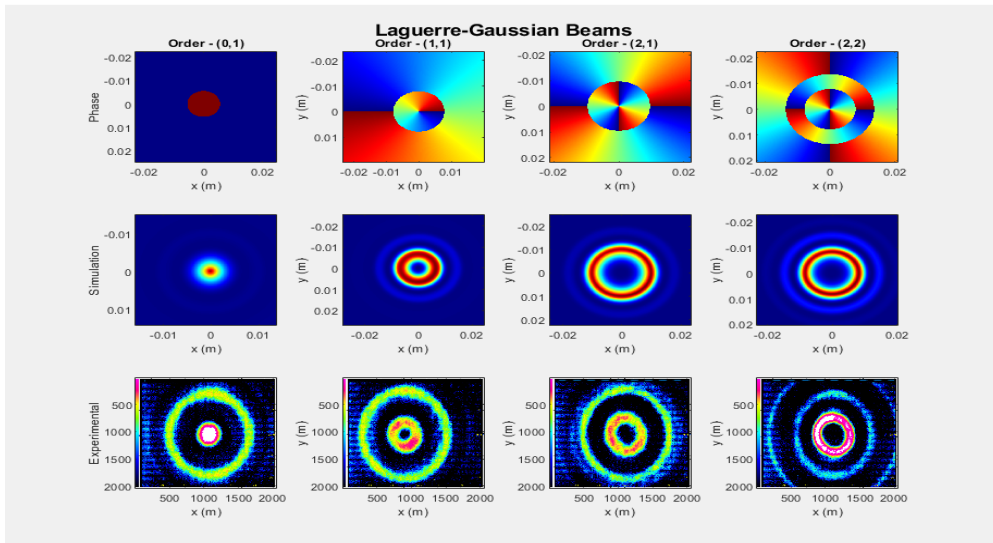


Figure 4-9 Improved L-G beams results – First row shows the phase mask used, blue-0 and red- $2\pi$ , second row shows the results, and the third one gives the experimental results. L-G orders: (0,1), (1,1), (2,1), (2,2) and scale parameters 100, 80, 85, 110 from the left to the right.



## Forked phase masks

Another way to improve the generation of beams carrying OAM is by using a forked phase mask. Here, we present the results obtained for a beam diffracted in the first order of this mask with  $l = 1$ , and its evolution as the number of divisions varies, consequently affecting the position of the first diffraction order. We can observe the emergence of a perfect ring characteristic of OAM with the increase in these divisions.

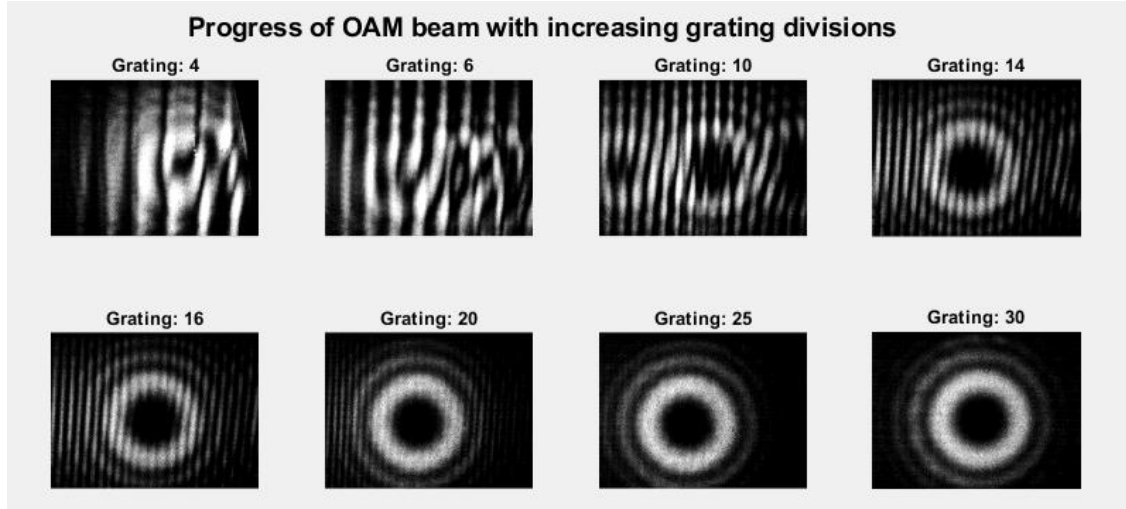


Figure 4-10 The progress of OAM-carrying beam with the increase of grating division in the forked phase mask,  $l=1$ .

Following the successful application of the forked phase mask, we proceeded to generate beams with higher-order OAM (OAM) up to  $l = 5$ , as depicted in Figure 4-11.

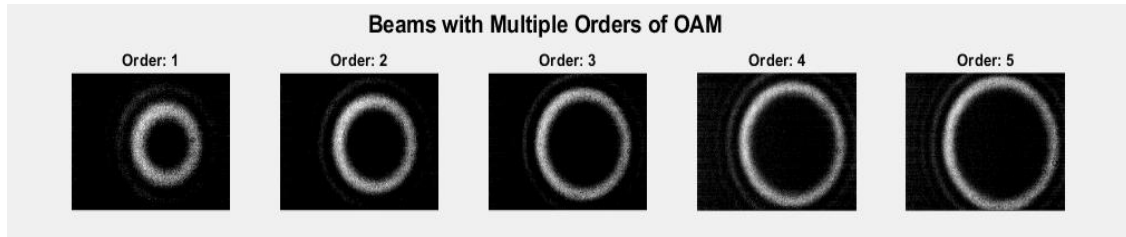


Figure 4-11 Beams carrying OAM, topological charges from 1 to 5.

## CHAPTER 5

# Conclusions

Throughout this study, we investigated and simulated the propagation of structured light for various beam types, including L-G, H-G, and B-G beams, as well as their relationship with beams carrying OAM. The generation of these beams was achieved using a SLM, and the OAM of the naturally occurring beams was evaluated, followed by refinement of their purity using forked phase masks. An experimental setup was designed to facilitate this generation, and a GUI was developed to streamline communication with the assembled setup. To visualize the intensity profile predictions for each beam, a numerical routine was created for beam propagation simulation. Both the numerical routine and the phase masks were integrated into the GUI and all of them were developed using MATLAB.

The results were satisfactory for H-G beams, which exhibit petal-like intensity patterns closely matching the experimental outcomes. For L-G and B-G beams, however, poor modulation was observed for modes carrying OAM. Although ring-shaped intensity patterns characteristic of OAM beams was observed, these rings were not even close to being perfectly circular but exhibited distortions. To address these distortions, forked phase masks were applied. Created by combining L-G masks with ramp masks. Using these masks, we observed a perfectly circular ring intensity profile characteristic of OAM.

The study concludes that while H-G beams can be generated with high accuracy using SLMs, generating high-purity L-G and B-G beams with OAM presents additional challenges due to the complexities of phase modulation and the inherent limitations of the SLM technology. The SLM can introduce distortions that are particularly problematic for beams with higher topological charges. To generate higher purity in OAM beams requires not only meticulous calibration of the SLM but also innovative solutions to compensate for its inherent limitations, such as advanced phase correction algorithms and the use of higher-resolution SLMs.

## 5.1 Future work

Moving forward in this research direction, several areas warrant focused attention. Firstly, exploring the generation and modulation of Airy beams represents a promising avenue. Airy beams exhibit. Additionally, investigating phase retrieval methods using Gerchberg-Saxton algorithms holds potential for generating phase masks that circumvent residual curvatures in the SLM and non-uniform pixel response. Furthermore, calibrating the gamma curve of the SLM could improve results, providing an improved phase modulation response of the SLM.

Regarding the main application proposed for that work, it is also essential to assess the resilience of OAM beams generated against adverse atmospheric conditions. Conducting experiments in controlled and real-world environments will provide insights into the effects of atmospheric turbulence and other environmental factors on the propagation and fidelity of structured light beams. Developing strategies to mitigate these effects will be crucial for practical applications in long-distance optical communication.

# References

- [1] K. Y. Bliokh *et al.*, “Roadmap on structured waves,” *Journal of Optics*, vol. 1, pp. 4, 2022.
- [2] M. Beijersbergen, R. J. C. Spreeuw, L. Allen, *et al.* “Orbital angular momentum of light and the transformation of Laguerre-Gaussian laser modes,” 1992.
- [3] H. Rubinsztein-Dunlop *et al.*, “Optical trapping of absorbing particles,” *Advances in Quantum Chemistry* 1998.
- [4] V. Yu. Barzhenov, M. V. Vasnetsov, and M. S. Soskin, “Laser beams with screw dislocation in their wavefronts,” *JETP Lett*, vol. 52, no. 8, 25 Oct. 1990.
- [5] J. E. Curtis, B. A. Koss, and D. G. Grier, “Dynamic Holographic Optical Tweezers,” *Optics Communications*, vol. 207, pp. 169-175, 2002.
- [6] H. D. Nguyen *et al.*, “Non-diffractive bessel beams for ultrafast laser scanning platform and proof-of-concept side-wall polishing of additively manufactured parts,” *Micromachines (Basel)*, vol. 11, 2020.
- [7] Y. Lian, X. Qi, Y. Wang, Z. Bai, Y. Wang, and Z. Lu, “OAM beam generation in space and its applications: A review,” *Optics and Lasers in Engineering*, vol. 151. Elsevier Ltd, Apr. 01, 2022.
- [8] E-karimi, “SAM and OAM interactions,” *Wikimedia Commons*. Accessed: Jul. 07, 2024.
- [9] A. H. Gnauck *et al.*, “Spectrally efficient long-haul WDM transmission using 224-Gb/s polarization-multiplexed 16-QAM,” *Journal of Lightwave Technology*, vol. 29, no. 4, pp. 373–377, 2011.
- [10] David J. Griffiths, “INTRODUCTION TO ELECTRODYNAMICS,” Pearson Education, 2013.
- [11] B. E. A. Saleh, “*Fundamentals of photonics.*,” John Wiley & Sons, 2019.
- [12] J. Sjöholm and K. Palmer, “Angular Momentum of Electromagnetic Radiation,” Uppsala, 2007.
- [13] C. J. Ahn, “An applicable 5.8 GHz wireless power transmission system with rough beamforming to Project Loon,” *ICT Express*, vol. 2, no. 2, pp. 87–90, Jun. 2016, doi: 10.1016/j.ict.2016.02.011.
- [14] F. Wu, Y. Luo, and Z. Cui, “A Systematic Summary and Comparison of Scalar Diffraction Theories for Structured Light Beams,” *Photonics*, vol. 10, no. 9, Sep. 2023, doi: 10.3390/photonics10091041.
- [16] E. Hecht, “*Optics*,” *Pearson Education Limited*, 2017.
- [17] J. D. Schmidt, “*Numerical simulation of optical wave propagation with examples in MATLAB.*,” SPIE, 2010.
- [18] X. Shu, L. Zhang, and I. Bennion, “Sensitivity Characteristics of Long-Period Fiber Gratings,” *Journal of Lightwave Technology*, vol. 20, no. 2, pp. 255-262, 2002.
- [19] S. Li, Q. Mo, X. Hu, C. Du, and J. Wang, “Controllable all-fiber orbital angular momentum mode converter,” *Opt Lett*, vol. 40, no. 18, p. 4376, Sep. 2015, doi: 10.1364/ol.40.004376.
- [20] L. Zhang, Y. Liu, X. Cao, and T. Wang, “High Sensitivity Chiral Long-Period Grating Sensors Written in the Twisted Fiber,” *IEEE Sens J*, vol. 16, no. 11, pp. 4253–4257, Jun. 2016.
- [21] Z. Huang *et al.*, “Excitation of high order orbital angular momentum modes in ultra-short chiral long period fiber gratings,” *Opt Express*, vol. 29, no. 24, p. 39384, Nov. 2021, doi: 10.1364/oe.442760.
- [22] X. Wei *et al.*, “Generation of arbitrary order Bessel beams via 3D printed axicons at the terahertz frequency range,” *Appl Opt*, vol. 54, no. 36, p. 10641, Dec. 2015, doi: 10.1364/ao.54.010641.
- [23] M. W. Beijersbergen, L. Allen *et al.*, “OPTICS COMMUNICATIONS Astigmatic laser mode converters and transfer of orbital angular momentum,” *Optics Communications*, vol. 96, pp 123-132, 1993.
- [24] M. J. Padgett and L. Allen, “The angular momentum of light: Optical spanners and the rotational frequency shift,” *Optical and Quantum Electronics*, vol. 31, no. 1. Springer Netherlands, pp. 1–12, 1999.
- [25] S. S. R. Oemrawsingh *et al.*, “Production and characterization of spiral phase plates for optical wavelengths,” *APPLIED OPTICS*, vol. 43, no. 3, 2004.
- [26] A. Rubano, F. Cardano, B. Piccirillo, and L. Marrucci, “Q-plate technology: a progress review [Invited],” *Journal of the Optical Society of America B*, vol. 36, no. 5, p. D70, May 2019.
- [27] E. Karimi *et al.*, “Efficient generation and sorting of orbital angular momentum eigenmodes of light by thermally tuned q -plates,” *Appl Phys Lett*, vol. 94, no. 23, 2009.
- [28] J. Hong, “Phase and polarization modulations based on LCOS SLM.”, St. Catherine College, 2021.
- [29] R. Santoso, “2D Optical Trapping Potential for the Confinement of Heteronuclear Molecules”, 2014.
- [30] Z. Zhao, “High Precision Optical Wavefront Generation Using Liquid Crystal Spatial Light Modulator (LC-SLM),” in *Liquid Crystals*, IntechOpen, 2022. doi: 10.5772/intechopen.100379.
- [31] F. Difato *et al.*, “Spatial light modulators for complex spatiotemporal illumination of neuronal networks,” *Neuromethods*, vol. 67, pp. 61–81, 2012, doi: 10.1007/7657\_2011\_3.
- [32] A. M. Yao and M. J. Padgett, “Orbital angular momentum: origins, behavior and applications,” *Adv Opt Photonics*, vol. 3, no. 2, p. 161, Jun. 2011, doi: 10.1364/aop.3.000161.
- [33] M. Padgett, “Light’s twist,” *Royal society publishing*, vol. 470, 2014.
- [34] M. Haddadi, “Graphical User Interface source code on GitHub,” Jul. 2024. [Online]. Available: <https://github.com/Mohaamedl/Physics-Project>